

First-principles investigations of arsenate doping into the ettringite lattice

Zhao, Yingliang; Sun, Yong; Guo, Zhenbang; Qiu, Jingping; Sun, Xiaogang

DOI

[10.1016/j.jclepro.2023.138266](https://doi.org/10.1016/j.jclepro.2023.138266)

Publication date

2023

Document Version

Final published version

Published in

Journal of Cleaner Production

Citation (APA)

Zhao, Y., Sun, Y., Guo, Z., Qiu, J., & Sun, X. (2023). First-principles investigations of arsenate doping into the ettringite lattice. *Journal of Cleaner Production*, 419, Article 138266.
<https://doi.org/10.1016/j.jclepro.2023.138266>

Important note

To cite this publication, please use the final published version (if applicable).
Please check the document version above.

Copyright

Other than for strictly personal use, it is not permitted to download, forward or distribute the text or part of it, without the consent of the author(s) and/or copyright holder(s), unless the work is under an open content license such as Creative Commons.

Takedown policy

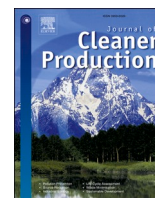
Please contact us and provide details if you believe this document breaches copyrights.
We will remove access to the work immediately and investigate your claim.

Green Open Access added to TU Delft Institutional Repository

'You share, we take care!' - Taverne project

<https://www.openaccess.nl/en/you-share-we-take-care>

Otherwise as indicated in the copyright section: the publisher is the copyright holder of this work and the author uses the Dutch legislation to make this work public.



First-principles investigations of arsenate doping into the ettringite lattice

Yingliang Zhao^{a,b}, Yong Sun^a, Zhenbang Guo^{a,c}, Jingping Qiu^{a,*}, Xiaogang Sun^a

^a College of Resources and Civil Engineering, Northeastern University, Shenyang, China

^b Department of Civil and Environmental Engineering, The Hong Kong Polytechnic University, Kowloon, Hong Kong

^c Faculty of Civil Engineering and Geosciences, Department of Hydraulic Engineering, Delft University of Technology, Delft, the Netherlands

ARTICLE INFO

Handling Editor: Zhen Leng

Keywords:

Ettringite
Arsenate
Elastic properties
First-principles calculations
Isomorphic substitution

ABSTRACT

Hazardous wastes are commonly immobilized using cementitious materials. Ettringite ($\text{Ca}_6\text{A}-\text{l}_2(\text{OH})_{12}(\text{SO}_4)_3 \cdot 26\text{H}_2\text{O}$) is one of the main components of hydrated cement and is known to stabilize anionic species. Thus, it is a promising material for the stabilization of arsenate (As(V)) in cementitious waste streams. However, the effects of As(V) incorporation into the ettringite structure on the structural properties of As and ettringite remain unclear. Herein, As(V) doping into the structure of ettringite was investigated based on the first-principles calculations using density functional theory (DFT), and the results suggested that the mechanism involving the substitution of AsO_4^{3-} by SO_4^{2-} was energetically favorable and that As doping increased the total bond order of ettringite, leading to a more stable structure. The elastic properties and anisotropy of ettringite and As-doped ettringite were also investigated using DFT calculations. The results showed that the mechanical properties of the As-doped ettringite structure were stable according to Born's criterion. Moreover, As doping increased the elastic constants and elastic modulus of ettringite but reduced its elastic anisotropy. These results provide valuable insights into the long-term stabilization of As species and their migration in cementitious wastes.

1. Introduction

As is a highly toxic element mainly generated in nonferrous metal processing. It poses serious environmental and human health risks (Liu et al., 2018; Min et al., 2019). China has high As-containing ore reserves (≈ 3.7 million tons), ranking first in the world (Li et al., 2016). More than 80% of the reserves exist in the form of symbiotic and associated As ores, such as Cu, Au, Zn, and Pb, which often leads to large quantities of As-containing wastes from metallurgical processes to produce the metal (Fei et al., 2018; Liang et al., 2017). Improper disposal of As-containing wastes leads to serious environmental problems. Thus, several countries, including China, have reported events of As poisoning (Ng et al., 2003; Tang et al., 2016). Therefore, it is necessary to develop a sustainable way to dispose of As-containing wastes.

Numerous immobilization strategies have been developed for hazardous waste disposal and prevention of its environment impact (Li et al., 2018b). Cement-based solidification/stabilization (S/S) technologies are attractive due to their simplicity and availability (Chen et al., 2009; Li et al., 2019). Hazardous wastes are mixed with a certain amount of cementitious materials to form stable matrices, restricting the

leaching of hazardous elements (Li et al., 2018a; Ouhadi et al., 2021; S. Wang, 2000). Currently, physical encapsulation and chemical stabilization are the main immobilization mechanisms in the process of hazardous waste immobilization by cementitious material treatments (Guo et al., 2017a). Physical encapsulation refers to encapsulating heavy metals into a low-permeability waste and isolating them from the environment. The physical encapsulation effects are highly dependent on the pore structure and permeability of the matrix (Wang et al., 2022b).

A chemical stabilization mechanism of the hazardous elements in cement has also been reported. Some hazardous ions can generate a relatively insoluble substance with low toxicity by reacting with the components in cementitious materials (Chrysochoou and Dermatas, 2006; Wang and Wang, 2022). For example, Cr(VI) can react with Ca^{2+} in the cement system to form calcium chromate precipitation and then reduce its leaching concentration (Zhang et al., 2018). Macphee et al. (Macphee and Glasser, 1993) found that Mn^{2+} , Ni^{2+} , and Cu^{2+} can exist as stable hydroxides at pH = 12–13. Moreover, a series of cementing gels produced in the reaction process of cementitious materials can produce chemical stabilization effects on hazardous elements (via surface

* Corresponding author.

E-mail address: qiujiaping@mail.neu.edu.cn (J. Qiu).

<https://doi.org/10.1016/j.jclepro.2023.138266>

Received 13 April 2023; Received in revised form 18 June 2023; Accepted 25 July 2023

Available online 26 July 2023

0959-6526/© 2023 Elsevier Ltd. All rights reserved.

Table 1
Lattice parameters of the ettringite and As-doped ettringite.

Lattice parameters	Length (Å)			Angles (°)			Bond length (Å)		Volume (Å ³)
	a	b	c	α	β	γ	S-O	As-O	
Ettringite	11.260	11.260	21.480	90.000	90.000	120.000	1.49 ± 0.014	–	2358.53
After GeomOpt	11.393	11.393	21.766	89.999	89.999	120.028	1.50 ± 0.001	–	2459.50
SM-I	11.468	11.467	21.708	89.811	90.191	120.432	1.50 ± 0.002	1.73 ± 0.023	2461.66
SM-II	11.485	11.446	21.722	90.153	89.915	120.410	1.50 ± 0.001	1.73 ± 0.005	2462.68
SM-III	11.454	11.649	21.664	89.684	90.285	120.851	1.50 ± 0.002	1.72 ± 0.024	2481.48

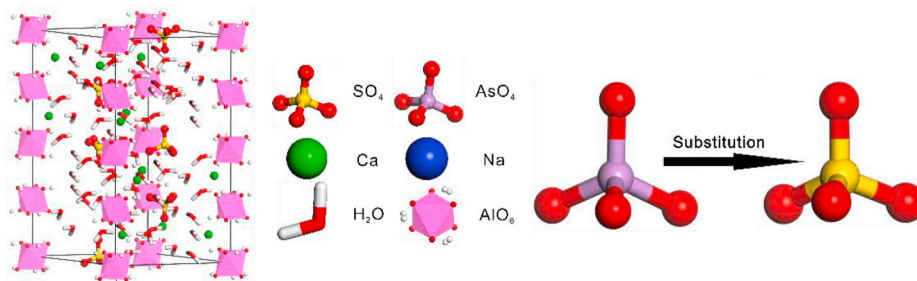


Fig. 1. Crystal structure of ettringite.

adsorption or/and ion substitution) (Baur and Johnson, 2003; Kersten; Tommaseo and Kersten, 2002). The different reaction products of cementitious materials exhibit various immobilization effects on the harmful elements; thus, the composition of the gelling system is directly dependent on the S/S effects.

At present, S/S technologies are widely employed for the disposal of As-containing waste using ordinary Portland cement (OPC) (Li et al., 2016; Liu et al., 2018; Min et al., 2019; Singh and Pant, 2006), and the hydration products, such as calcium silicate hydrate (C–S–H) and the ettringite ($3\text{CaO}\cdot\text{Al}_2\text{O}_3\cdot 3\text{CaSO}_4\cdot 32\text{H}_2\text{O}$) phases, contribute to the As immobilization (Gougar et al., 1996; Myneni et al., 1998). C–S–H is generally an amorphous phase with numerous micropores and high surface area (Zhang et al., 2021, 2022). C–S–H was reported to effectively adsorb As species (Phenrat et al., 2005; Stronach et al., 1997).

Ettringite, which has a hexagonal prismatic shape, is another main reaction product generated during OPC hydration. In the crystal structure of ettringite, columns of $[\text{Al}(\text{OH})_6]^{3-}$ octahedra are linked together by Ca^{2+} and OH^- ions, and the SO_4^{2-} and H_2O molecules are located on the outer surface of the columns (Karen Scrivener, 2016; Meier and Plank, 2016). The special structure of ettringite facilitates the replacement of SO_4^{2-} by oxygen-containing anions with similar structures and sizes, such as VO_4^{3-} , CrO_4^{2-} , SeO_4^{2-} , IO_3^- , and AsO_4^{3-} (Guo et al., 2017a, 2017b, 2019; Saslow et al., 2020). Phenrat et al. (2005) used scanning electron microscopy and X-ray diffraction to study the effects of the S/S technology on As-containing wastes using Portland cement and lime; the results indicated that the As species could be adsorbed onto the C–S–H

surface and replace the SO_4^{2-} of the ettringite. The AsO_4^{3-} complexes in the ettringite structure were also evaluated by Myneni et al. (1998) by using Raman and Fourier transform infrared spectroscopies. However, to the best of the authors' knowledge, limited studies have focused on the changes in the structure and mechanical properties of the ettringite caused by As doping, which is crucial to understand the long-term stabilization effects of the As species in cementitious wastes.

Therefore, herein, the structure of As(V) incorporated in the ettringite lattice was investigated via density functional theory (DFT) modeling. The possible incorporation modes of As(V) in the crystal structure of ettringite were investigated via energy minimization. The effects of As(V) incorporation on the lattice parameters and interatomic bonding of ettringite were then analyzed. The effects of As(V) incorporation on the elastic properties, including elastic constants, elastic modulus, and elastic anisotropy, were also assessed.

2. Methods

The general formula of ettringite used in this work is $\text{Ca}_6\text{Al}_2(\text{OH})_{12}(\text{SO}_4)_3\cdot 26\text{H}_2\text{O}$ (Manzano et al., 2012); its lattice parameters are listed in Table 1. Fig. 1 shows the crystal structure of ettringite. The figure indicates that AsO_4^{3-} has a similar structure to SO_4^{2-} ; thus, theoretically, isomorphic substitution could occur between them. Generally, there are three substitution modes.

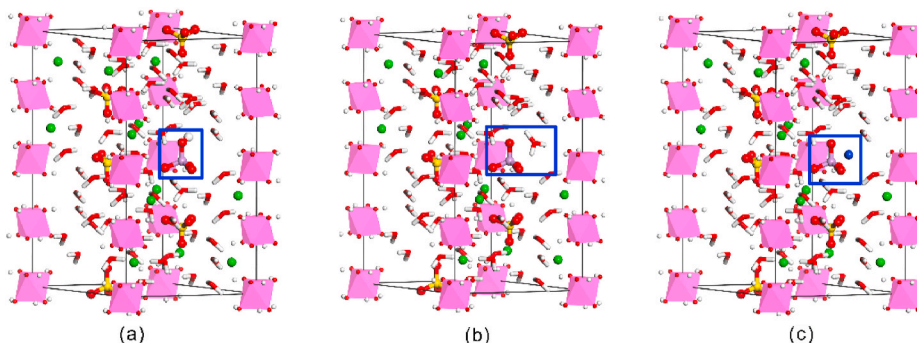


Fig. 2. The doping patterns of As(V) in ettringite: (a) SM-I-, (b) SM-II-, and (c) SM-III-doped ettringite.

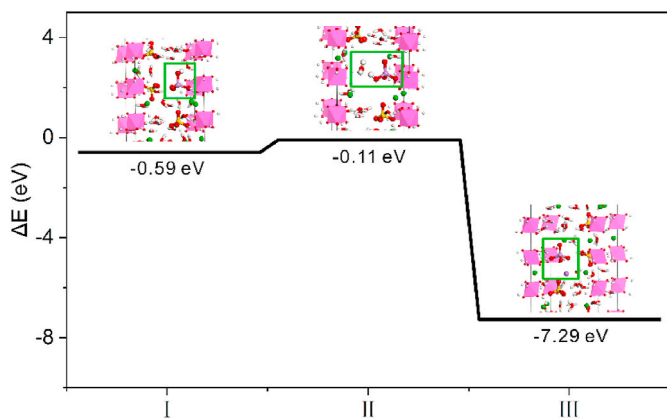


Fig. 3. Substitution energy of different substitution configurations.

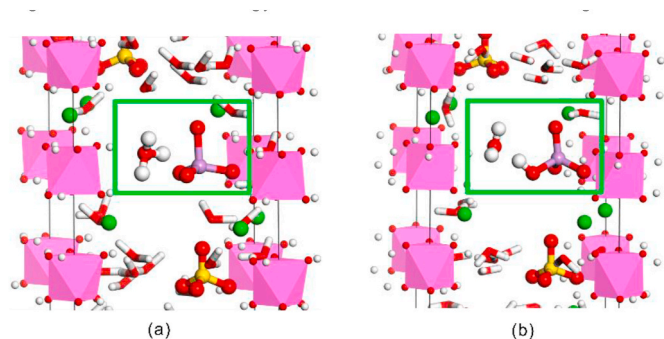


Fig. 4. Crystal configuration of SM-II-doped ettringite (a) before the geometry optimization and (b) after the geometry optimization.

- (1) One SO_4^{2-} in ettringite is substituted by AsO_4^{3-} and one O in AsO_4^{3-} is protonated to balance the charge (substitution mode I, SM-I, Fig. 2a).
- (2) One SO_4^{2-} in ettringite is substituted by AsO_4^{3-} and one O in an adjacent water molecule is protonated to balance the charge (substitution mode II, SM-II, Fig. 2b).
- (3) One SO_4^{2-} in ettringite is substituted by AsO_4^{3-} and one Na^+ is simultaneously introduced into the ettringite structure to balance the charge (substitution mode III, SM-III, Fig. 2c).

DFT calculations were performed using the CASTEP module in Materials studio 8.0 (Accelrys Inc.). Perdew–Burke–Ernzerhof Generalized Gradient Approximation (PBE-GGA) was used in the calculations as the exchange functional to calculate the exchange-correlation energy (Fernández-Martínez et al., 2008). Broyden Fletcher Goldfarb Shanno was employed to optimize the atomic positions (Vanderbilt, 1990). Ultrasoft pseudopotential was used to describe the electron–ion interactions (Vanderbilt, 1990). The convergence thresholds for interatomic forces, stress, and displacement were $0.03 \text{ eV } \text{Å}^{-1}$, 0.05 GPa ,

and 0.001 Å , respectively. The convergence threshold of the total energy change and self-consistent iteration accuracy were set as 1.0×10^{-5} and $1.0 \times 10^{-6} \text{ eV} \cdot \text{atom}^{-1}$, respectively. Based on the convergence tests and previous works (Scholtzová et al., 2015b), the kinetic energy cut-off used in the calculations was 600 eV . To balance the number of calculations and their efficiency, the Γ point was used for sampling in the Brillouin region (Scholtzová et al., 2015a, 2015b).

The substitution energy (ΔE) was calculated according to Eq. (1):

$$\Delta E = E_{\text{ettringite+As}} + E_{\text{As}} - E_{\text{SO}_4^{2-}} - E_{\text{ettringite}}, \# \quad (1)$$

where $E_{\text{ettringite+As}}$, E_{As} , and $E_{\text{SO}_4^{2-}}$ are the energies of the As-doped ettringite, AsO_4^{3-} , and SO_4^{2-} , respectively.

3. Results and discussion

3.1. Energy and crystal structures

The calculation results of the substitution energies are shown in Fig. 3. The substitution energies of the SM-I, SM-II, and SM-III doping were -0.59 , -0.11 , and -7.29 eV , respectively, indicating that from an energy perspective, the three substitution modes can occur. Additionally, the substitution energy of SM-III was significantly lower than those of the other two substitution configurations; thus, SM-III doping can occur more easily. Fig. 4 shows the crystal structure of the SM-II-doped ettringite after geometric optimization. As shown in Fig. 4, after the geometric optimization of the SM-II-doped ettringite, a proton exited the protonated H_2O molecule and protonated an O atom in AsO_4^{3-} , which is similar to the SM-I doping mechanism. Therefore, the three substitution configurations can be reduced to two types (i.e., SM-I and SM-III doping).

Table 1 shows the cell parameters of the ettringite and As-doped ettringite. The data in the table shows that compared with ettringite, the As doping increased the volume of the ettringite crystals, among which the volume of SM-I and SM-III increased by approximately 0.088% and 0.89% , respectively. This increase was mainly due to the larger size of AsO_4^{3-} compared with SO_4^{2-} . This phenomenon is in accordance with the results obtained by Wang et al. (2017), who found that the volume of As-doped gypsum crystals increased by 0.12% – 0.47% compared with that of undoped gypsum crystals.

Moreover, compared to undoped ettringite, As doping caused slight deformation in the ettringite crystals, which is reflected in the side length and angle of the crystal structure. For example, doping ettringite with As increased the γ angle (Table 1). Compared with undoped ettringite, the γ angle of the SM-I- and SM-III-doped ettringite increases by approximately 0.34% and 0.69% , respectively. The changes in these parameters by As doping directly change the ettringite crystal structure and affect its micro- and macro properties.

In contrast, the average bond length of the S–O bond ($\approx 1.50 \text{ Å}$) did not change before and after the As doping, indicating that the introduction of As did not significantly change the structure of SO_4^{2-} in ettringite. In addition, the average bond length of As–O bond is 1.72 – 1.73 Å , which is consistent with the research results obtained by

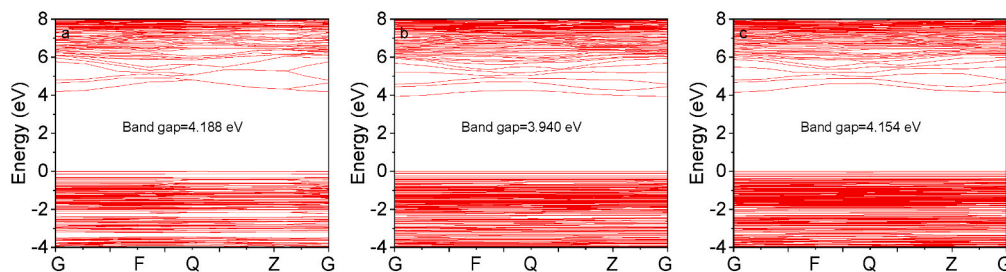


Fig. 5. Band structures of (a) ettringite as well as (b) SM-I- and (c) SM-III-doped ettringite.

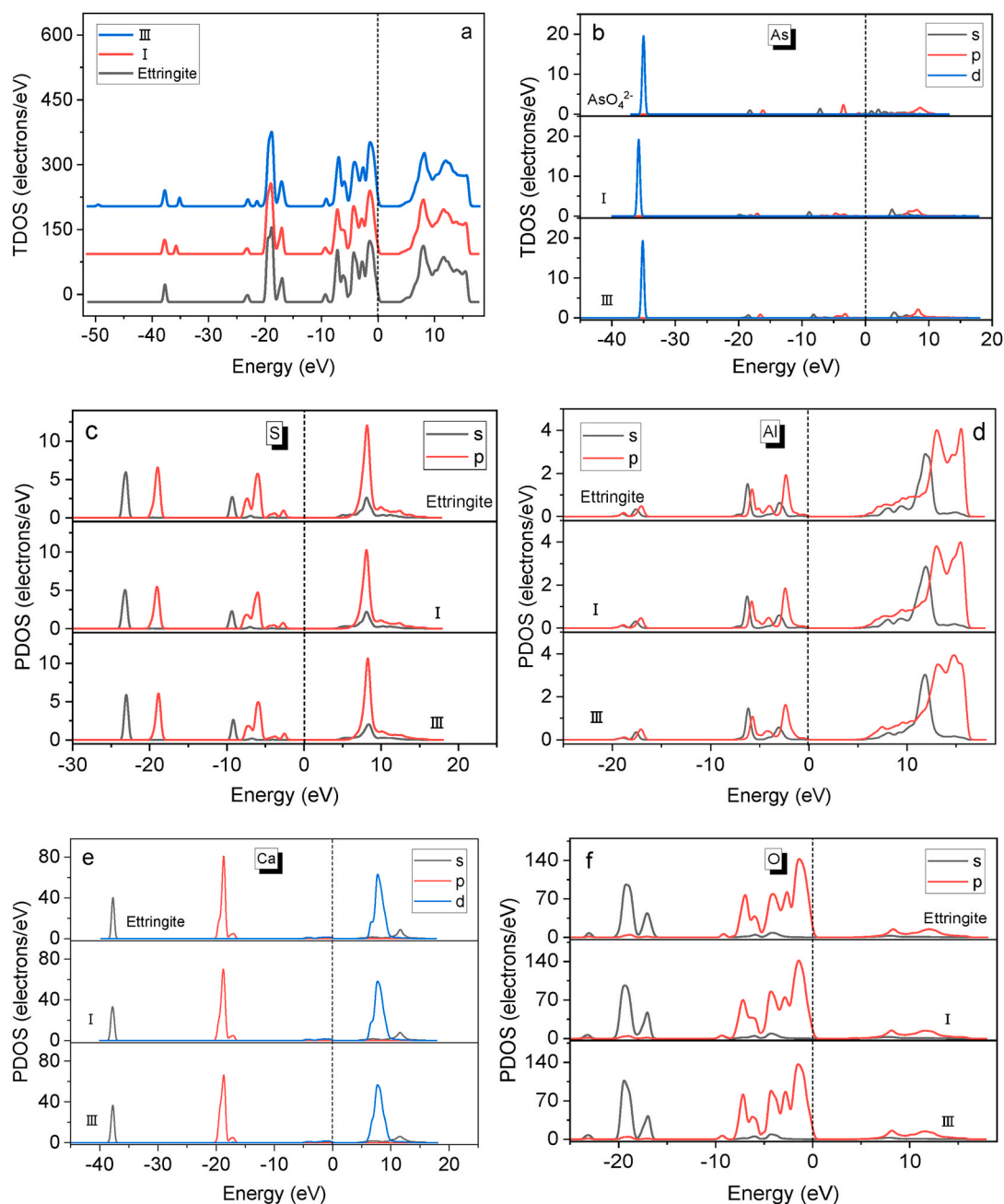


Fig. 6. (a) Total density of states (TDOS) and (b–f) partial density of states (PDOS) of ettringite and the As-doped ettringite.

Wang et al. (2017) and Alejandro et al. (Fernández-Martínez et al., 2008).

3.2. Electronic structures

Fig. 5 shows the calculation results of the band structure of ettringite and the As-doped ettringite. As shown in Fig. 5, the band gaps of ettringite, SM-I-doped ettringite, and SM-III-doped ettringite were 4.188, 3.940, and 4.154 eV, respectively. The obtained band gap of ettringite is consistent with the calculation results of San et al. (2018), in which the band gap was approximately 4.20 eV. When As was introduced into ettringite, the periodic potential field near the dopant ions was disturbed and an additional binding state was formed, resulting in a change in the energy levels.

The conductive properties of materials are dependent on the band gap. The band gaps of insulating and conducting materials are

approximately 3–6 and 0.1–2 eV, respectively (Li Haitao, 2016). Therefore, both ettringite and the As-doped ettringite exhibited typical insulator characteristics. Additionally, the band gap is an important index to evaluate the stability of crystalline materials. Generally, smaller band gaps facilitate the jump of electrons from valence bands to conduction bands, resulting in a material that is more sensitive to external stimuli such as light, heat, and friction (Yedukondalu et al., 2012).

The density of states are used to represent the number of electron states per unit energy interval, which reflect the energy distribution of electrons in the reaction system as well as the material electronic properties (Toriyama et al., 2022). Fig. 6a shows the total density of states diagram of ettringite and the As-doped ettringite. The figure indicates that after As doping, a relatively clear d-orbital peak of As was observed at approximately -35 eV. Fig. 6b shows the partial density of states of As before and after doping. The figure shows that after the As doping into ettringite, its orbital peak shifted to a low energy state by

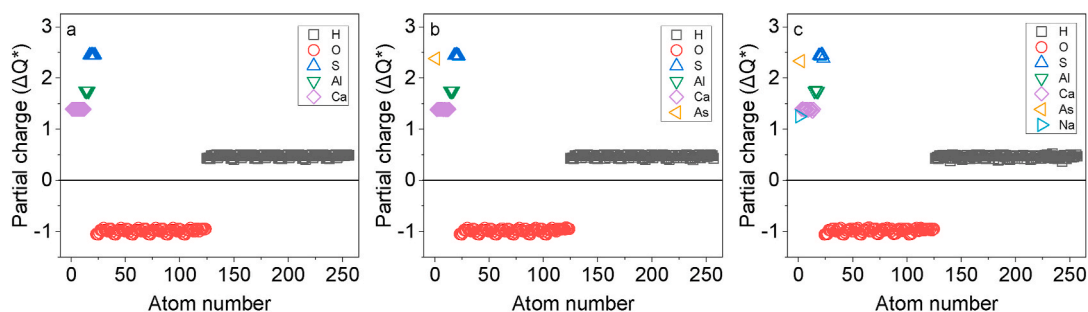


Fig. 7. Distribution of partial charge of elements in (a) ettringite as well as (b) SM-I- (c) and SM-III-doped ettringite.

Table 2

Average partial charge of elements in ettringite as well as SM-I- and SM-III-doped ettringite.

Element	H	O	S	Al	Ca	As	Na
Ettringite	0.474	-0.988	2.447	1.745	1.390	–	–
SM-I	0.469	-0.985	2.440	1.745	1.386	2.380	–
SM-III	0.460	-0.982	2.430	1.745	1.385	2.330	1.250

approximately 0.2–0.8 eV, and its p-orbital peak intensity significantly decreased, indicating that the system becomes more stable.

Fig. 7 shows the partial charge distribution (ΔQ^*) of atoms in ettringite, SM-I, and SM-III. The average local charges of elements are listed in Table 2. As shown in Fig. 7, all atoms in ettringite and the As-doped ettringite, except the O atom, have positive local charges.

According to Table 2, the average local charges of H, O, S, Al, and Ca in ettringite are 0.474, -0.988, 2.447, 1.745, and 1.390, respectively, which is consistent with the results of a previous work (San et al., 2018). Moreover, after As doping, the average local charges of the H, S, and Ca atoms in ettringite decreased, whereas the average local charge of the O atom was negative and increased after As doping, indicating that As doping caused charge redistribution in the ettringite crystal. In contrast, the average local charge of the Al atom did not change before and after the As doping. The average local charge of As in SM-I and SM-III was

2.380 and 2.330, respectively. The lower local charge of As in SM-III may be due to the partial charge balance caused by the introduction of Na.

3.3. Interatomic bonding

Fig. 8 shows the distribution of bond length and bond order in ettringite and the As-doped ettringite, as well as the contribution percentage of chemical bonds to the total bond order. As shown in Fig. 8a–c, the bond lengths of the strong covalent O–H and S–O bonds in ettringite were approximately 1 and 1.5 Å, respectively; their bond orders were distributed around 0.4–0.6, which is in good agreement with the results of previous studies (San et al., 2018). The bond order of the Ca–O bond was less than 0.1 and its bond length was 2.2–2.7 Å, indicating lower covalency.

Overall, the relationship between bond length and bond order exhibited a slight change after As doping. The As–O bond was mainly observed in strong covalent bonds. In SM-III, the bond order of As–O was greater than 0.5 and its bond length was approximately 1.7 Å, whereas in SM-I, one of the As–O bond order was approximately 0.3 and its bond length was approximately 1.8 Å, which can be attributed to the hydroxylation of the O atom in the As–O bond. Moreover, the bond order of S–O bond slightly increased, indicating the increase in covalency of the S–O bond after As doping.

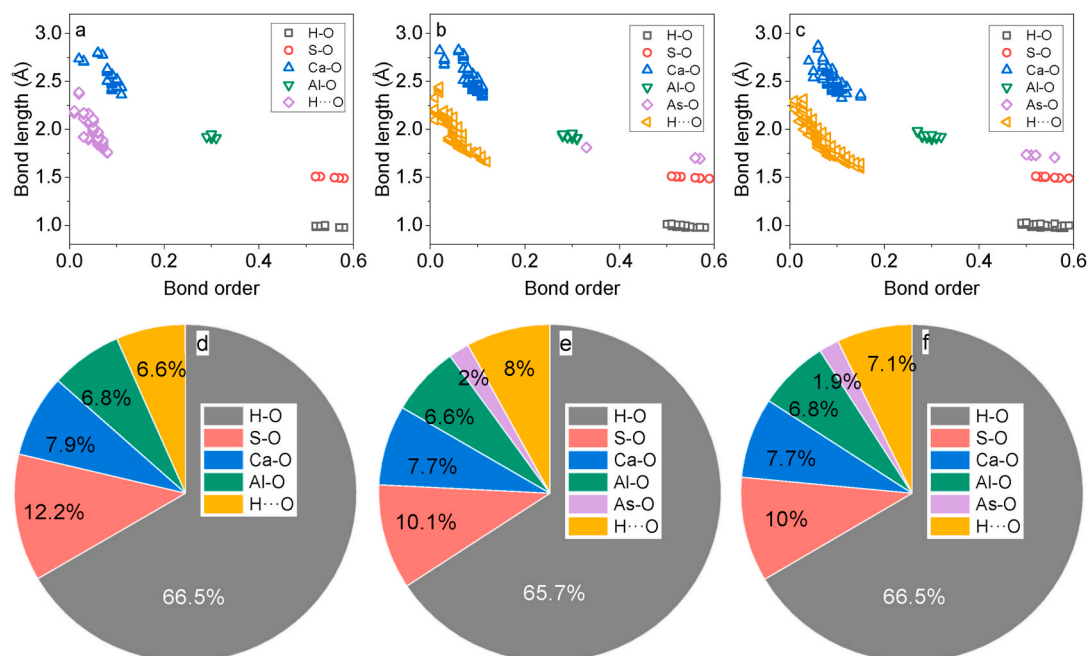


Fig. 8. (a–c) Bond order vs. bond length distribution and (d–f) percentage contribution to the total bond order for (a, d) ettringite as well as (b, e) SM-I- and (c, f) SM-III-doped ettringite.

Table 3

Bond-order statistics in ettringite as well as the SM-I- and SM-III-doped ettringite.

Sample	H–O	S–O	Ca–O	Al–O	As–O	H...O	Total
Ettringite	70.32	12.87	8.34	7.20	–	6.94	105.67
SM-I	70.86	10.69	8.21	7.20	2.02	7.60	106.58
SM-III	70.41	10.77	8.20	7.11	2.09	8.53	107.11

Table 4

H-bonds statistics in ettringite as well as the SM-I- and SM-III-doped ettringite.

Sample	Quantity	Average length (Å)	Max length (Å)	Min length (Å)
Ettringite	366	2.557	3.097	1.755
SM-I	349	2.531	3.096	1.662
SM-III	338	2.525	3.094	1.595

The total bond order in ettringite and the As-doped ettringite are listed in Table 3, and Fig. 8d–f shows the proportion of each bond order. The total bond order of the H–O bond slightly increased after As doping (Table 3) compared with the Ca–O and Al–O bonds, which slightly decreased. The decrease in the total bond order of S–O was mainly caused by the substitution of AsO_4^{2-} for SO_4^{2-} . The increase in the total bond order of the H...O bond was more clear, indicating that the hydrogen bond changed more significantly after As doping.

The number of hydrogen bonds as well as the average bond lengths in the crystal structures of ettringite and the As-doped ettringite are listed in Table 4. The data in the table indicate that As doping reduced the number of hydrogen bonds in ettringite, mainly because the S atom in the substituted SO_4^{2-} could also form hydrogen bond with the H atom. Additionally, the average bond length of hydrogen bond decreased by As doping, leading to an elevated interaction force between H and O (S), which is consistent with the elevated bond order of the H...O bonds (Table 3).

In addition, the data listed in Table 3 indicate that the total bond order of chemical bonds in ettringite increased after As doping. The total bond order in undoped ettringite was approximately 105.67, which increased to 106.58 and 107.11 in cases of SM-I and SM-III, respectively. Bond order is used in molecular orbital theory to indicate the bonding strength of two adjacent atoms. Typically, larger bond orders indicate higher bond energies and more stable molecules. The increase in the

Table 5

Calculated mechanical properties of ettringite and the As-doped ettringite (GPa).

NO.	C_{11}	C_{12}	C_{13}	C_{14}	C_{33}	C_{44}	C_{66}	B^a	G	E	ν	B/G	A^t	Ref.	
Ettringite	34.35	20.63	8.69	0.08	52.06	8.61	16.15	21.94	11.33	29.01	0.28	1.94	0.38	–	
SM-I	44.71	18.97	11.11	1.21	66.04	14.93	16.14	26.29	16.33	40.59	0.24	1.61	0.13	–	
SM-III	53.60	10.86	9.01	–2.25	58.73	16.58	12.89	24.85	17.76	43.03	0.21	1.40	0.15	–	
Other works (for ettringite)	50.25	22.39	21.00	0.28	65.40	18.08	13.81	32.55	16.54	42.44	0.28	1.97	–	(San et al., 2018) ^b	
	39.50	25.70	19.70	0.10	57.10	10.00	6.90	29.40	9.60	26.00	0.35	3.06	0.16	(Scholtzová et al., 2015b) ^c	
	45.40	25.00	23.00	1.90	53.90	11.10	8.10	26.70	12.40	–	0.30	2.15	–	(Liu et al., 2012) ^d	
	36.50	18.50	18.31	0.18	49.86	12.06	8.85	25.57	10.63	28.00	0.32	2.41	–	(Sarkar et al., 2019) ^e	
	44.03	22.34	19.28	0.48	63.89	9.12	9.07	29.70	9.86	26.62	0.35	3.01	–	(S. Hajilar and B. Shafei, 2014) ^f	
	55.26	26.10	14.62	0.99	141.96	8.13	14.61	16.08	37.79	42.25	0.31	0.43	–	(S. Hajilar and B. Shafei, 2014) ^g	
	73.68	34.54	32.89	–0.93	198.28	14.89	17.79	22.62	55.15	59.69	0.32	0.41	–	(S. Hajilar and B. Shafei, 2014) ^h	
	36.60	19.00	15.90	–	47.50	9.30	10.70	24.70	9.20	24.50	0.34	2.68	–	(Honorio et al., 2020) ⁱ	
	–	–	–	–	–	–	–	–	29.96	12.57	33.08	0.32	2.38	0.51	(Manzano et al., 2012) ^j
	Experimental (for ettringite)	35.1 ± 0.1	21.9 ± 0.1	20.0 ± 0.5	0.6 ± 0.2	55 ± 1	11.0 ± 0.2	6.6 ± 0.1	27.3 ± 0.9	9.5 ± 0.8	25.0 ± 2	0.34 ± 0.02	2.87	0.53	Speziale et al. (2008)

Note: a, Bulk modulus (B), Shear modulus (G), Young's modulus (E), and Poisson's ratio (ν); b, calculated by VASP; c, calculated by VASP; d, calculated by ReaxFF; e, calculated by Interface FF; f, calculated by COMPASS FF; g, Universal FF; h, calculated by Dreiding; i, calculated by AFFF; and j, calculated by DFT.

total bond order of ettringite after As doping might indicate an increase in its stability, which is in good agreement with the energy reduction of ettringite after As doping (Fig. 3).

3.4. Elastic constant and elastic modulus

The degree of deformation of a material under applied stress is usually indicated by its elastic properties. According to the continuum mechanics principle, the stress on the material and the resulting strain satisfies the generalized Hooke's law, given by Eq. (2).

$$\sigma_{ij} = C_{ij}\epsilon_j \quad (i, j = 1, 2, \dots, 6), \quad (2)$$

where σ_{ij} is the stress tensor and C_{ij} is the elastic constant.

The space group of ettringite belongs to the trigonal system ($P31C$), and its elastic constant C_{ij} has six independent nonzero elements: C_{11} , C_{12} , C_{13} , C_{14} , C_{33} , C_{44} , and C_{66} , where $C_{66} = (C_{11} - C_{12})/2$ (Scholtzová et al., 2015b). The C_{ij} matrix is given by Eq. (3). Although the symmetry of $P31C$ was no longer strictly satisfied after As doping, the elastic constant of the As-doped ettringite can still (for convenience) be explained based on the symmetry of the $P31C$ trigonal system. This method has been reported in previous studies (Ansari and Malakpour, 2015; Li Jun, 2020; Rashko et al., 2023; Ruiz-Puigdollers and Gamallo, 2017; Wang et al., 2022a).

$$C = \begin{bmatrix} C_{11} & C_{12} & C_{13} & C_{14} & 0 & 0 \\ C_{12} & C_{11} & C_{13} & -C_{14} & 0 & 0 \\ C_{13} & C_{13} & C_{33} & 0 & 0 & 0 \\ C_{14} & -C_{14} & 0 & C_{44} & 0 & 0 \\ 0 & 0 & 0 & 0 & C_{44} & C_{14} \\ 0 & 0 & 0 & 0 & C_{14} & C_{66} \end{bmatrix}. \quad (3)$$

Brillouin spectroscopy has been used to measure the experimental results of the elastic constants of ettringite (Speziale et al., 2008). In this study, DFT was used to calculate the elastic constants of ettringite and the As-doped ettringite via energy minimization; the results are listed in Table 5. Previous calculations and experimental results of the elastic constants of ettringite were also presented as controls. As shown in Table 5, the calculation results of the present work are in good agreement with the experimental values and calculation results from previous

studies, indicating the rationality of the calculation methods presented in this study.

As indicated by Eqs. (4)–(7), the mechanical stability of ettringite and the As-doped ettringite can be judged by Born's criterion (Li Jun, 2020). According to the data in Table 5, the elastic constants of both ettringite and the As-doped ettringite satisfied Born's criterion, indicating that they were mechanically stable (Zhang et al., 2008a, 2008d).

$$C_{11} - |C_{12}| > 0, \quad (4)$$

$$(C_{11} + C_{12})C_{13} - 2(C_{13})^2 > 0, \quad (5)$$

$$(C_{11} - C_{12})C_{44} - 2(C_{14})^2 > 0, \quad (6)$$

and

$$C_{44} > 0. \quad (7)$$

Generally, C_{11} , C_{22} , and C_{33} reflect the uniaxial compression properties of crystalline materials along the x , y , and z axes, respectively (Bao et al., 2019). The results in Table 5 show that C_{33} and C_{11} were larger than other elastic constants, indicating the strong compression resistance of ettringite along the x and z axes under uniaxial compression. C_{33} was higher than C_{11} , indicating the stronger compressibility of ettringite along the x axis. This can be attributed to the orientation of $[\text{Al}(\text{OH})_6]^{3-}$ octahedral in ettringite, which is distributed along the z axis, leading to stronger rigidity in this direction (Speziale et al., 2008). C_{44} and C_{66} correspond to the shear resistance along the $[001]$ and $[110]$ directions, respectively, on the (100) plane. C_{12} reflects the shear resistance along the $[1\bar{1}0]$ direction on the (110) plane (Liu Xiangjun, 2021). The results listed in Table 5 indicate the anisotropy of the shear modulus of ettringite due to the different values of C_{44} , C_{66} , and C_{12} . In addition, the difference among C_{44} , C_{66} , and C_{12} was higher than that between C_{11} and C_{33} , which indicates that the anisotropy of the shear modulus of ettringite was stronger than that of its bulk modulus. However, As doping relatively changed the elastic constants of ettringite, and the values of C_{33} and C_{11} were still higher than other elastic constants, which suggests that As doping did not change the compression direction of ettringite. Moreover, As doping led to an increase in the C_{33} and C_{11} values. In SM-I- and SM-III-doped ettringite, C_{11} increased by approximately 30.16% and 56.04% respectively, whereas C_{33} increased by approximately 30.16% and 56.04%, respectively. This suggests that the compressibility of the As-doped ettringite increases along the x and z axes.

As doping led to more significant effects on C_{44} than the previously discussed C_{ij} s. In the case of SM-I- and SM-III-doped ettringite, C_{44} increased by approximately 74.30% and 92.57%, respectively. This indicates that the shear resistance increased along the $[001]$ direction on the (100) plane. However, As doping led to insignificant changes in C_{66} of the SM-I-doped ettringite, but a reduction of approximately 20.19% was observed in the SM-III-doped ettringite, suggesting a decrease in the shear resistance along the $[110]$ direction on the (100) plane.

The mechanical properties of materials, such as brittleness, hardness, and strength, are dependent on their elastic modulus. According to the first principle calculations, the polycrystalline modulus of ettringite was calculated using the Vogit–Reuss–Hill (VRH) method (Hill, 1952). The Vogit approximation assumes homogeneity and strain distribution, whereas the Reuss approximation assumes uniform stress distribution. Thus, crystal moduli calculated using these approximations are overestimated (Voigt, 1910) and underestimated (Voigt, 1910), respectively. Hill comprehensively considered the shortcomings of Vogit and Reuss and proposed that the average value of the two is closer to the measured value (Hill, 1952).

The bulk modulus (B) of a crystalline material is the relationship between the bulk strain and volume stress when certain pressure is applied to the material, reflecting the resistance of the material under external pressure equalization (Sun Haofang, 2020). Shear modulus (G)

refers to the ratio of the shear stress to shear strain applied when elastic deformation occurs in a material, which represents the ability of a material to resist shear deformation (Yedukondalu et al., 2012). Generally, materials with higher shear modulus are more rigid. The bulk modulus (B) and shear modulus (G) are calculated using Eqs. (8) and (9) (Honorio et al., 2020).

$$B = \frac{B_v + B_R}{2} \quad (8)$$

and

$$G = \frac{G_v + G_R}{2}, \quad (9)$$

where the subscripts v and R represent Vogit and Reuss approximations, respectively.

B_v , G_v , B_R , and G_R can be calculated using Eqs. (12)–(13).

$$9B_v = (C_{11} + C_{22} + C_{33}) + 2(C_{12} + C_{13} + C_{23}), \quad (10)$$

$$\frac{1}{B_R} = (S_{11} + S_{22} + S_{33}) + 2(S_{12} + S_{13} + S_{23}), \quad (11)$$

$$15G_v = (C_{11} + C_{22} + C_{33}) - (C_{12} + C_{23} + C_{31}) + 3(C_{44} + C_{55} + C_{66}), \quad (12)$$

and

$$\frac{1}{G_R} = 4(S_{11} + S_{22} + S_{33}) - 4(S_{12} + S_{23} + S_{31}) + 3(S_{44} + S_{55} + S_{66}), \quad (13)$$

where $[S_{ij}] = [C_{ij}]^{-1}$ is the compliance coefficient.

Young's modulus (E), which is mainly used to characterize the stiffness of the material, is the ratio of stress to strain in the same direction when a material is subjected to a linear stress (Jiang Wenwu, 2021). Poisson's ratio (ν) is the ratio of transverse strain to longitudinal strain when stress is applied to a material in one direction. Young's modulus and Poisson's ratio can be calculated using Eqs. (14) and (15) (Hill, 1952).

$$E = \frac{9BG}{3B + G} \quad (14)$$

and

$$\nu = \frac{3B - 2G}{6B + 2G} \quad (15)$$

The calculation results of bulk modulus, shear modulus, Young's modulus, and Poisson's ratio of ettringite and the As-doped ettringite are listed in Table 5.

As shown in Table 5, the bulk modulus, shear modulus, Young's modulus and Poisson's ratio of ettringite were 21.94, 11.33, 29.01, and 0.28 GPa, respectively, which is in good agreement with previous studies, indicating the rationality of this calculation method. As doping has a significant effect on the elastic modulus of ettringite. As shown in Table 5, the bulk modulus, shear modulus, and Young's modulus of the SM-I-doped ettringite are 26.29, 16.33, and 40.59 GPa, respectively, which are approximately 19.83%, 44.13%, and 39.92% higher than those of the undoped ettringite. In the case of SM-III, the bulk modulus, shear modulus, and Young's modulus of ettringite are 24.85, 17.76, and 43.03 GPa, respectively, which are approximately 13.26%, 56.75%, and 48.33% higher than those of the undoped ettringite. The increase in bulk modulus indicates that the compression resistance of ettringite after As doping is stronger under external uniform compression, which is in good agreement with the changes in C_{11} and C_{33} caused by As doping. Shear modulus is proportional to the rigidity of the material; thus, As-doped ettringite exhibits a strong shear strain resistance and strong rigidity. Higher values of Young's modulus indicate stronger tensile and

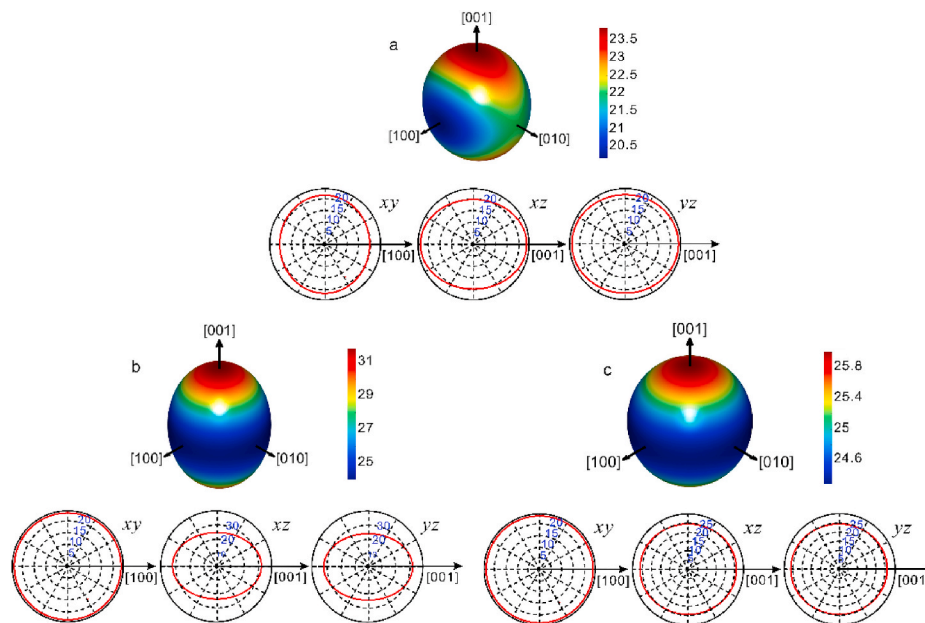


Fig. 9. Anisotropy of bulk modulus: (a) ettringite as well as (b) SM-I- and (c) SM-III-doped ettringite.

compressive resistances. Therefore, As-doped ettringite is not easily deformed when subjected to external pressure.

Additionally, the Poisson's ratio of a stable crystal material ranges from -1.0 to 0.5 . Under zero pressure, the material was ductile when $\nu > 0.26$ and was brittle when $\nu < 0.26$ (Hadi et al., 2022). As shown in Table 5, the Poisson's ratio of ettringite is 0.28 ; thus, ettringite is a ductile material. As doping significantly reduces the Poisson's ratio of ettringite. The Poisson's ratios of SM-I- and SM-III-doped ettringite were 0.24 and 0.21 , respectively, which are approximately 14.29% and 25.00% lower than those of undoped ettringite. In this case, ettringite is a brittle material and its ductility is reduced. In addition, the decrease in the Poisson's ratio indicates that when ettringite is deformed in a certain direction, the deformation perpendicular to this direction decreases, and the increase in the elastic modulus is generally accompanied by an increase in the material brittleness (Huang et al., 2019).

The ratio of bulk modulus to shear modulus (B/G) is called the Pugh toughness coefficient (An and Goddard, 2014), which is used to characterize the toughness of materials. Generally, the B/G value of a brittle material is lower than 1.75 , whereas that of a ductile material is higher than 1.75 . As shown in Table 5, the B/G value of undoped ettringite was 1.94 , indicating that it is a ductile material, which is in good agreement with the results reported in previous studies. The B/G values of SM-I and SM-III were 1.61 and 1.40 , respectively, suggesting that As-doped ettringite is a brittle material, which is consistent with the change in the ν attributed to As doping.

According to the above analysis, As doping led to an increase in the bulk modulus, shear modulus, and Young's modulus of ettringite. At the microscopic level, the bonding properties of crystals determine their mechanical properties (Domnich et al., 2011; Li Jun, 2020). Bulk modulus depends on the average bond strength in the crystal material,

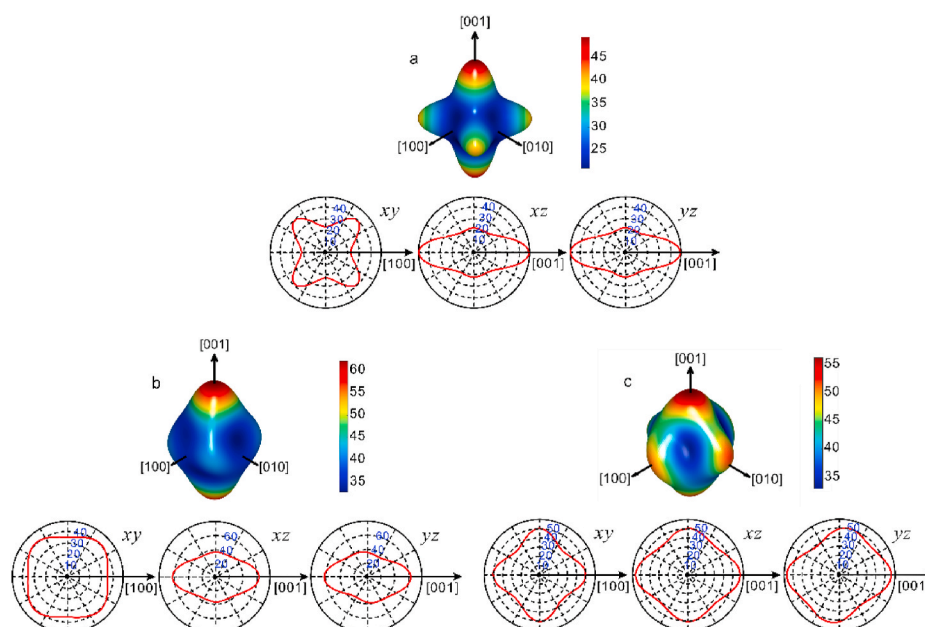


Fig. 10. Anisotropy of Young's modulus: (a) ettringite as well as (b) SM-I- and (c) SM-III-doped ettringite.

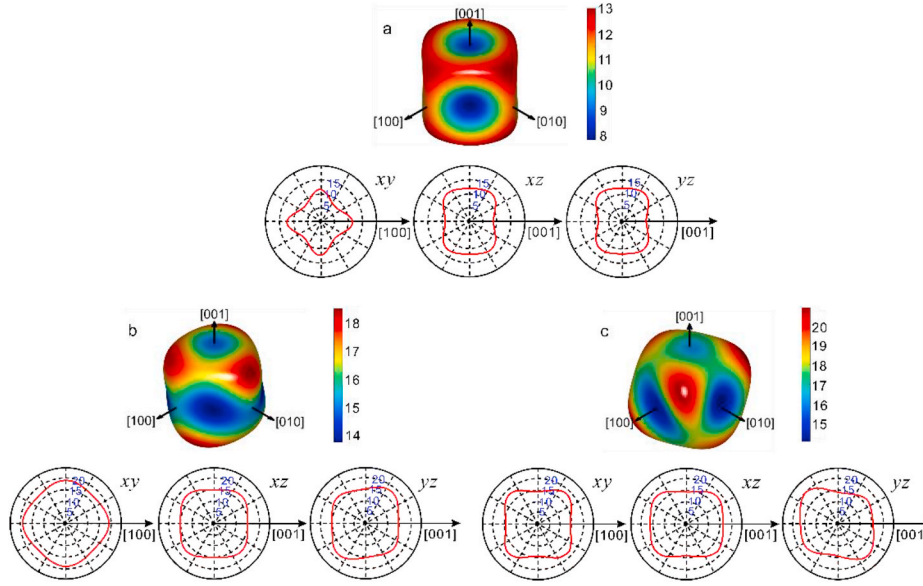


Fig. 11. Anisotropy of shear modulus: (a) ettringite as well as (b) SM-I- and (c) SM-III-doped ettringite.

which also reflects the ability of the crystal to resist the deformation of the bond length (Sun Haofang, 2020; Yedukondalu et al., 2012) from a microscopic perspective. Shear modulus reflects the ability of the bond angle in the crystal material to resist a change (Yedukondalu et al., 2012). Young's modulus depends on the bonding mode, chemical composition, and crystal structure of the material (Jiang Wenwu, 2021). The analysis results of Section 3.3 indicate that As doping leads to an increase in the total bond order of the chemical bonds in ettringite. This indicates an increase in the interaction energy between atoms, increasing the ability of ettringite to resist external forces.

3.5. Elastic anisotropy

Anisotropy exists in a wide variety of materials. Anisotropy in a crystal refers to its ability to have different properties in different directions, that is, the properties of the material depend on the direction. This concept is distinct from material inhomogeneity, which refers the change in the material properties depending on the location in the material. The elastic properties of most materials are anisotropic, which is similar to the mechanical properties of the strength yield point, crack, and phase transition behavior (Li Jun, 2020). The anisotropic factor (A^L) can be calculated using Eq. (16) (Güler et al., 2022b; Shah et al., 2023). $A^L = 0$ suggests that a material is isotropic. The larger the difference between A^L and 0, the more significant the anisotropy of the material.

$$A^L = \sqrt{5 \left[\ln \left(\frac{G_V}{G_R} \right) \right]^2 + \left[\ln \left(\frac{B_V}{B_R} \right) \right]^2}. \quad (16)$$

The A^L values of ettringite before and after As doping are listed in Table 5. The A^L values of ettringite as well as the SM-I- and SM-III-doped ettringite were 0.38, 0.13, and 0.15, respectively. Therefore, the descending order of anisotropy is ettringite > SM-III > SM-I.

In the trigonal system, the relationship of the bulk modulus and Young's modulus with crystal direction is expressed by Eqs. (17) and (18) (Nye, 1985; Zhang et al., 2008b, 2008c).

$$\frac{1}{B} = (S_{11} + S_{12} + S_{13}) - (S_{11} + S_{12} - S_{13} - S_{33})l_3^2 \quad (17)$$

and

$$\frac{1}{E} = (1 - l_3^2)^2 S_{11} + l_3^4 S_{33} + l_3^2 (1 - l_3^2) (2S_{13} + S_{44}) + 2l_2 l_3 (3l_1^2 - l_2^2) S_{14} + 2l_1 l_3 (3l_2^2 - l_1^2) S_{23}, \quad \# \quad (18)$$

where S_{ij} is the elastic compliance constant, l_i is the direction cosines, and $l_1^2 + l_2^2 + l_3^2 = 1$ ($l_1, l_2, \text{ and } l_3 \in [0, 1]$).

Figs. 9–11 shows the relationship of the bulk modulus, shear modulus, and Young's modulus with the crystal direction (the figure was drawn using ElasticPOST) (Liao et al., 2018). The anisotropy of crystal elasticity can be assessed based on the deviation between the three-dimensional graph of bulk modulus, shear modulus, and Young's modulus and the sphere. The anisotropy increases with the increase in the deviation between the three-dimensional graph and sphere (Güler et al., 2022a; Li Jun, 2020).

As shown in Fig. 9, the three-dimensional patterns of the bulk modulus are slightly different from the sphere. Moreover, among the three types of ettringite, the three-dimensional patterns of SM-III exhibited the least difference from the sphere, and their projections on the xy , xz , and yz planes were all circular, indicating that the lowest anisotropy was obtained for the bulk modulus of the SM-III-doped ettringite.

Based on the projection of the bulk modulus of ettringite on the xy , xz , and yz planes, the bulk modulus is isotropic in the xy and yz planes, whereas the anisotropy in the xz plane is more significant than that in the other two planes and its magnitude changes with the direction. The bulk modulus of the SM-I-doped ettringite is isotropic in the xy plane but anisotropic in the xz and yz planes. Notably, the plane projection of the bulk modulus shows that As doping increased the maximum value of the bulk modulus along the x and z axes, indicating that As doping enhanced the compression resistance of ettringite along the x and z axes.

Fig. 10 shows the three-dimensional patterns of the Young's modulus. As shown in Fig. 10, the three-dimensional patterns significantly differed from the sphere, suggesting that the Young's modulus included high anisotropy. As doping decreased the anisotropy in the Young's modulus. Moreover, after As doping, the maximum value of the Young's modulus increased along the x and z axes, indicating that the resistance of ettringite to deformation was enhanced along the x and z directions after As doping.

Fig. 11 shows the relationship between the shear modulus and crystal orientation. Its deviation from the sphere is larger than that of the bulk modulus but smaller than that of Young's modulus. Therefore, the

anisotropy of the shear modulus is intermediate between those of the bulk modulus and Young's modulus, which is in good agreement with the previous analysis of elastic constants. This means that the difference among C_{44} , C_{66} , and C_{12} is higher than that between C_{11} and C_{33} (the anisotropy of shear modulus is greater than that of bulk modulus). In the case of ettringite, the projection of shear modulus on the plane showed that the maximum value of shear modulus along the z axis is lower than that along the x axis and As doping relatively reduces the anisotropy of shear modulus. Additionally, the maximum value of shear modulus along the x and z axis increases after As doping, indicating that the shear resistance of ettringite along the x and z axes increased after the As doping.

4. Conclusions

In this study, we investigated the impact of As doping on the structure and mechanical properties of ettringite using the first-principles method. Our findings demonstrate that AsO_4^{3-} can substitute SO_4^{2-} in the ettringite structure due to its negative substitution energies. This substitution resulted in a volumetric expansion of ettringite by up to 0.89%. Furthermore, the elastic modulus of ettringite increased upon As doping, attributed to the enhanced total bond order of the chemical bonds within ettringite. These results suggest that As-doped ettringite exhibits improved resistance to deformation. However, it is important to note that while the microstructure of the material influences its macroscopic properties, the relationship between them is not necessarily one-to-one. Therefore, future research should focus on establishing a comprehensive understanding of the relationship between the microstructure of As-doped ettringite and its macroscopic properties.

CRedit authorship contribution statement

Yingliang Zhao: Data curation, Writing – original draft. **Yong Sun:** Visualization, Investigation. **Zhenbang Guo:** Supervision. **Jingping Qiu:** Conceptualization, Methodology. **Xiaogang Sun:** Supervision.

Declaration of competing interest

The authors declare that they have no known competing financial interests or personal relationships that could have appeared to influence the work reported in this paper.

Data availability

Data will be made available on request.

Acknowledgement

The authors would like to thank the supports of National Natural Science Foundation of China (Key Program), 52234004. Moreover, the authors would like to thank Yao Fan from Shiyanjia Lab (www.shiyanjia.com) for the cloud computing services.

References

- An, Q., Goddard, W.A., 2014. Microalloying boron carbide with silicon to achieve dramatically improved ductility. *J. Phys. Chem. Lett.* 5, 4169–4174.
- Ansari, R., Malakpour, S., 2015. Structural and elastic properties characterization of Be and Mg doped boron nitride nanotubes using DFT calculations. *Superlattice. Microst.* 82, 113–123.
- Bao, L., Qu, D., Kong, Z., Duan, Y., 2019. Anisotropies in elastic properties and thermal conductivities of trigonal TM₂C (TM = V, Nb, Ta) carbides. *Solid State Sci.* 98, 106027.
- Baur, I., Johnson, C., 2003. The solubility of selenate-AFT (3CaO·Al₂O₃·3CaSeO₄·37.5H₂O) and selenate-AFM (3CaO·Al₂O₃·CaSeO₄·xH₂O). *Cement Concr. Res.* 33, 1741–1748.
- Chen, Q.Y., Tyrer, M., Hills, C.D., Yang, X.M., Carey, P., 2009. Immobilisation of heavy metal in cement-based solidification/stabilisation: a review. *Waste Manag.* 29, 390–403.
- Chrysochoou, M., Dermatas, D., 2006. Evaluation of ettringite and hydrocalumite formation for heavy metal immobilization: literature review and experimental study. *J. Hazard Mater.* 136, 20–33.
- Domnich, V., Reynaud, S., Haber, R.A., Chhowalla, M., 2011. Boron carbide: structure, properties, and stability under stress. *J. Am. Ceram. Soc.* 94, 3605–3628.
- Fei, J., Wang, T., Zhou, Y., Wang, Z., Min, X., Ke, Y., Hu, W., Chai, L., 2018. Aromatic organoarsenic compounds (AOCs) occurrence and remediation methods. *Chemosphere* 207, 665–675.
- Fernández-Martínez, A., Cuello, G.J., Johnson, M.R., Bardelli, F., Román-Ross, G., Charlet, L., Turrillas, X., 2008. Arsenate incorporation in gypsum probed by neutron, X-ray scattering and density functional theory modeling. *J. Phys. Chem. A* 112, 5159–5166.
- Gougar, M., Scheetz, B.E., Roy, D.M., 1996. Ettringite and C S H Portland cement phases for waste ion immobilization: a review. *Waste Manag.* 16, 295–303.
- Güler, E., Uğur, Ş., Güler, M., Uğur, G., 2022a. Exploring the elastic, mechanical and anisotropic response of Ti-5Al-XSn alloys through DFT calculations. *Chin. J. Phys.* 77, 151–160.
- Güler, E., Uğur, Ş., Güler, M., Uğur, G., 2022b. Exploring the elastic, mechanical and anisotropic response of Ti-5Al-XSn alloys through DFT calculations. *Chin. J. Phys.* 77, 151–160.
- Guo, B., Liu, B., Yang, J., Zhang, S., 2017a. The mechanisms of heavy metal immobilization by cementitious material treatments and thermal treatments: a review. *J. Environ. Manag.* 193, 410–422.
- Guo, B., Sasaki, K., Hirajima, T., 2017b. Selenite and selenate uptaken in ettringite: immobilization mechanisms, coordination chemistry, and insights from structure. *Cement Concr. Res.* 100, 166–175.
- Guo, B., Xiong, Y., Chen, W., Saslow, S.A., Kozai, N., Ohnuki, T., Dabo, I., Sasaki, K., 2019. Spectroscopic and first-principles investigations of iodine species incorporation into ettringite: implications for iodine migration in cement waste forms. *J. Hazard Mater.*, 121880
- Hadi, M.A., Christopoulos, S.-R.G., Chronoes, A., Naqib, S.H., Islam, A.K.M.A., 2022. DFT insights into the electronic structure, mechanical behaviour, lattice dynamics and defect processes in the first Sc-based MAX phase Sc(2)SnC. *Sci. Rep.* 12, 14037.
- Hajilar, S., Shafei, B., 2014. Nano-scale characterization of elastic properties of Aft and AFm phases of hydrated cement paste. *Computational Modelling of Concrete Structures* 299–306.
- Hill, R., 1952. The elastic behaviour of a crystalline aggregate. *Proc. Phys. Soc.* 65, 349–354.
- Honorio, T., Guerra, P., Bourdot, A., 2020. Molecular simulation of the structure and elastic properties of ettringite and monosulfoaluminate. *Cement Concr. Res.* 135, 106126.
- Huang, X., Li, S., Jin, Y., Yang, D., Su, G., He, X., 2019. Analysis on the influence of Poisson's ratio on brittle fracture by applying uni-bond dual-parameter peridynamic model. *Eng. Fract. Mech.* 222, 106685.
- Jiang, Wenwu, 2021. First-principles Calculation and Energy Storage Application of Cobalt Sulfide. Master, Changsha.
- Kersten, M. *Aqueous Solubility Diagrams for Cementitious Waste Stabilization Systems. vol. 1. The C-S-H Solid-Solution System.*
- Li, Haitao, 2016. First-Principles Study on Microstructures and Elastic Properties of Clay Minerals. Doctor, Taiyuan.
- Li, Jun, 2020. First-Principles Study of Mechanical Behaviors and Toughening Mechanisms of Boron Carbide. Doctoral, Wuhan.
- Li, Y.-C., Min, X.-B., Chai, L.-Y., Shi, M.-Q., Tang, C.-J., Wang, Q.-W., Liang, Y.-J., Lei, J., Liyang, W.-J., 2016. Co-treatment of gypsum sludge and Pb/Zn smelting slag for the solidification of sludge containing arsenic and heavy metals. *J. Environ. Manag.* 181, 756–761.
- Li, S., Huang, X., Muhammad, F., Yu, L., Xia, M., Zhao, J., Jiao, B., Shiau, Y., Li, D., 2018a. Waste solidification/stabilization of lead-zinc slag by utilizing fly ash based geopolymers. *RSC Adv.* 8, 32956–32965.
- Li, Y.-C., Min, X.-B., Ke, Y., Chai, L.-Y., Shi, M.-Q., Tang, C.-J., Wang, Q.-W., Liang, Y.-J., Lei, J., Liu, D.-G., 2018b. Utilization of red mud and Pb/Zn smelter waste for the synthesis of a red mud-based cementitious material. *J. Hazard Mater.* 344, 343–349.
- Li, Y., Min, X., Ke, Y., Fei, J., Liu, D., Tang, C., 2019. Immobilization potential and immobilization mechanism of arsenic in cemented paste backfill. *Miner. Eng.* 138, 101–107.
- Liang, Y., Min, X., Chai, L., Wang, M., Liyang, W., Pan, Q., Okido, M., 2017. Stabilization of arsenic sludge with mechanochemically modified zero valent iron. *Chemosphere* 168, 1142–1151.
- Liao, M., Liu, Y., Min, L., Lai, Z., Han, T., Yang, D., Zhu, J., 2018. Alloying effect on phase stability, elastic and thermodynamic properties of Nb-Ti-V-Zr high entropy alloy. *Intermetallics* 101, 152–164.
- Liu, Xiangjun, 2021. Study on the Occurrence State of Rare Earth Ce in Steel and its Influence Mechanism of Mechanical Properties and Corrosion Properties of Steel. Doctoral, Baotou.
- Liu, L., Jaramillo-Botero, A., Goddard, W.A., Sun, H., 2012. Development of a ReaxFF reactive force field for ettringite and study of its mechanical failure modes from reactive dynamics simulations. *J. Phys. Chem. A* 116, 3918–3925.
- Liu, D.-G., Min, X.-B., Ke, Y., Chai, L.-Y., Liang, Y.-J., Li, Y.-C., Yao, L., Wang, Z.-B., 2018. Co-treatment of flotation waste, neutralization sludge, and arsenic-containing gypsum sludge from copper smelting: solidification/stabilization of arsenic and heavy metals with minimal cement clinker. *Environ. Sci. Pollut. Control Ser.* 25, 7600–7607.
- Macphee, D.E., Glasser, F.P., 1993. Immobilization science of cement systems. *MRS Bull.* 18, 66–71.

- Manzano, H., Ayuela, A., Telesca, A., Monteiro, P.J.M., Dolado, J.S., 2012. Ettringite strengthening at high pressures induced by the densification of the hydrogen bond network. *J. Phys. Chem. C* 116, 16138–16143.
- Meier, M.R., Plank, J., 2016. Crystal growth of $[\text{Ca}_3\text{Al}(\text{OH})_6\cdot 12\text{H}_2\text{O}]_2\cdot (\text{SO}_4)_3\cdot 2\text{H}_2\text{O}$ (ettringite) under microgravity: on the impact of anionicity of polycarboxylate comb polymers. *J. Cryst. Growth* 446, 92–102.
- Min, X.-B., Liu, D.-G., Chai, L.-Y., Ke, Y., Liang, Y.-J., Shi, M.-Q., Li, Y.-C., Tang, C.-J., Wang, Y.-Y., Wang, Z.-B., 2019. Comparison of arsenic immobilization properties among calcium silicate hydrate, ettringite, and friedel's salt in a slag-based binder. *Environ. Prog. Sustain. Energy* 38, S422–S428.
- Myneni, S.C., Traina, S.J., Waychunas, G.A., Logan, T.J., 1998. Vibrational spectroscopy of functional group chemistry and arsenate coordination in ettringite. *Geochem. Cosmochim. Acta* 62, 3499–3514.
- Ng, J.C., Wang, J., Shraim, A., 2003. A global health problem caused by arsenic from natural sources. *Chemosphere* 52, 1353–1359.
- Nye, J.F., 1985. *Physical Properties of Crystals: Their Representation by Tensors and Matrices*. Oxford university press.
- Ouhadi, V.R., Yong, R.N., Deiranlou, M., 2021. Enhancement of cement-based solidification/stabilization of a lead-contaminated smectite clay. *J. Hazard Mater.* 403, 123969.
- Phenrat, T., Marhaba, T.F., Rachakornkij, M., 2005. A SEM and X-ray study for investigation of solidified/stabilized arsenic-iron hydroxide sludge. *J. Hazard Mater.* 118, 185–195.
- Rashko, M.N., Hamad, A.H., Othman, M.S., 2023. Impacts of doping cadmium atoms on the mechanical properties of (n,0) zigzag SWCNTs: DFT approach. *Diam. Relat. Mater.* 133, 109681.
- Ruiz-Puigdollers, A., Gamallo, P., 2017. DFT study of the role of N- and B-doping on structural, elastic and electronic properties of α -, β - and γ -graphyne. *Carbon* 114, 301–310.
- S Wang, C., 2000. Solidification/stabilization of Cr(VI) with cement: leachability and XRD analyses. *Cement Concr. Res.* 30, 385–389.
- San, S., Li, N., Tao, Y., Zhang, W., Ching, W.-Y., 2018. Understanding the atomic and electronic origin of mechanical property in thaumasite and ettringite mineral crystals. *J. Am. Ceram. Soc.* 101, 5177–5187.
- Sarkar, P.K., Mitra, N., Prasad, D., 2019. Molecular level deformation mechanism of ettringite. *Cement Concr. Res.* 124, 105836.
- Saslow, S.A., Kerisit, S.N., Varga, T., Mergelsberg, S.T., Corkhill, C.L., Snyder, M.M.V., Avalos, N.M., Yorkshire, A.S., Bailey, D.J., Crum, J., Asmussen, R.M., 2020. Immobilizing perchlorate in ettringite via sulfate substitution. *Environ. Sci. Technol.* 54, 13610–13618.
- Scholtzová, E., Kucková, L., Kožíšek, J., Tunega, D., 2015a. Structural and spectroscopic characterization of ettringite mineral –combined DFT and experimental study. *J. Mol. Struct.* 1100, 215–224.
- Scholtzová, E., Tunega, D., Speziale, S., 2015b. Mechanical properties of ettringite and thaumasite—DFT and experimental study. *Cement Concr. Res.* 77, 9–15.
- Scrivener, Karen (Ed.), 2016. *A Practical Guide to Microstructural Analysis of Cementitious Materials*. Taylor & Francis Group.
- Shah, M., Nuruzzaman, M., Hossain, A., Jubair, M., Zilani, M., 2023. A DFT insight into structural, mechanical, elasto-acoustic, and anisotropic properties of AePdH_3 (Ae = Ca, Sr, Ba) perovskites under pressure. *Computational Condensed Matter* 34, e00774.
- Singh, T.S., Pant, K.K., 2006. Solidification/stabilization of arsenic containing solid wastes using portland cement, fly ash and polymeric materials. *J. Hazard Mater.* 131, 29–36.
- Speziale, S., Jiang, F., Mao, Z., Monteiro, P.J., Wenk, H.-R., Duffy, T.S., Schilling, F.R., 2008. Single-crystal elastic constants of natural ettringite. *Cement Concr. Res.* 38, 885–889.
- Stronach, S.A., Walker, N.L., Macphree, D.E., Glasser, F.P., 1997. Reactions between cement and As(III) oxide: the system $\text{CaO}-\text{SiO}_2-\text{As}_2\text{O}_3-\text{H}_2\text{O}$ at 25°C. *Waste Manag.* 17, 9–13.
- Sun, Haofang, 2020. *Study on the Stability of Phases and the First Principle in Nickel-Based Superalloys*. Doctoral, Shenyang.
- Tang, Z., Guo, Z., Zhou, L., Xue, S., Zhu, Q., Zhu, H., 2016. Combined and relative effect levels of perceived risk, knowledge, optimism, pessimism, and social trust on anxiety among inhabitants concerning living on heavy metal contaminated soil. *Int. J. Environ. Res. Publ. Health* 13, 1076.
- Tommaseo, C.E., Kersten, M., 2002. Aqueous solubility diagrams for cementitious waste stabilization systems. 3. Mechanism of zinc immobilization by calcium silicate hydrate. *Environ. Sci. Technol.* 36, 2919–2925.
- Toriyama, M.Y., Ganose, A.M., Dylla, M., Anand, S., Park, J., Brod, M.K., Munro, J.M., Persson, K.A., Jain, A., Snyder, G.J., 2022. How to analyse a density of states. *Materials Today Electronics* 1, 100002.
- Vanderbilt, 1990. Soft self-consistent pseudopotentials in a generalized eigenvalue formalism. *Phys. Rev. B* 41, 7892–7895.
- Voigt, W., 1910. *Lehrbuch der kristallphysik:(mit ausschluss der kristalloptik)*. BG Teubner.
- Wang, D., Wang, Q., 2022. Clarifying and quantifying the immobilization capacity of cement pastes on heavy metals. *Cement Concr. Res.* 161, 106945.
- Wang, S., Zhang, D., Ma, X., Zhang, G., Jia, Y., Hatada, K., 2017. Spectroscopic and DFT study on the species and local structure of arsenate incorporated in gypsum lattice. *Chem. Geol.* 460, 46–53.
- Wang, J., Zhao, J., Qiao, Y., Luan, Z., 2022a. Effect of Mg(II), Mn(II), and Fe(II) doping on the mechanical properties and electronic structure of calcite. *Mater. Today Commun.* 31, 103725.
- Wang, Z., Wang, Y., Wu, L., Wu, A., Ruan, Z., Zhang, M., Zhao, R., 2022b. Effective reuse of red mud as supplementary material in cemented paste backfill: durability and environmental impact. *Construct. Build. Mater.* 328, 127002.
- Yedukondalu, N., Ghule, V.D., Vaitheeswaran, G., 2012. Computational study of structural, electronic, and optical properties of crystalline NH_4N_3 . *J. Phys. Chem. C* 116, 16910–16917.
- Zhang, J.-M., Yang, Y., Xu, K.-W., Ji, V., 2008a. Mechanical stability and strength of a single Au crystal. *Can. J. Phys.* 86, 935–941.
- Zhang, J.-M., Yang, Y., Xu, K.-W., Ji, V., 2008b. Mechanical stability and strength of a single Au crystal. *Can. J. Phys.* 86, 935–941.
- Zhang, J.-M., Zhang, Y., Xu, K.-W., Ji, V., 2008c. General compliance transformation relation and applications for anisotropic cubic metals. *Mater. Lett.* 62, 1328–1332.
- Zhang, J.-M., Zhang, Y., Xu, K.-W., Ji, V., 2008d. General compliance transformation relation and applications for anisotropic cubic metals. *Mater. Lett.* 62, 1328–1332.
- Zhang, M., Yang, C., Zhao, M., Yu, L., Yang, K., Zhu, X., Jiang, X., 2018. Immobilization of Cr(VI) by hydrated Portland cement pastes with and without calcium sulfate. *J. Hazard Mater.* 342, 242–251.
- Zhang, Y., Zhou, Q., Ju, J.W., Bauchy, M., 2021. New insights into the mechanism governing the elasticity of calcium silicate hydrate gels exposed to high temperature: a molecular dynamics study. *Cement Concr. Res.* 141, 106333.
- Zhang, Y., Zhang, S., Jiang, X., Chen, Q., Jiang, Z., Ju, J.W., Bauchy, M., 2022. Insights into the thermal effect on the fracture toughness of calcium silicate hydrate grains: a reactive molecular dynamics study. *Cement Concr. Compos.* 134, 104824.